Observation of non-reciprocal wave propagation in a dynamic phononic lattice

Yifan Wang [1,+]*, Behrooz Yousefzadeh* [1,+]*, Hui Chen* [2]*, Hussein Nassar* [2]*, Guoliang Huang* [2]*, Chiara Daraio* [1]

[1] Division of Engineering and Applied Science, California Institute of Technology, Pasadena, CA, 91125, USA

[2] Department of Mechanical and Aerospace Engineering, University of Missouri, Columbia, MO, 65211, USA

[+] Y.W. and B.Y. contributed equally to this work.

Phononic crystals and metamaterials control acoustic waves through the geometry of their building blocks, engineered with periodic impedance mismatches and/or local resonances[1-7]. The majority of current realizations focus on designing metamaterials in their spatial dimensions, while the material properties remain unchanged over time. This design framework restricts the application of metamaterials in scenarios where material's tunability and adaptivity is required[8,9]. Here we demonstrate realization of a dynamic phononic lattice in which the elastic properties can vary over time with spatiotemporal modulation. This time dependence leads to novel wave propagation behaviors such as non-reciprocity[10-12], which is very difficult to achieve in time-invariant systems. Though we focus on elastic waves in a magnetically coupled lattice, the concept extends to other types of waves such as thermal diodes[13] and photonic systems[14]. Our system behaves as a mechanical diode operating at tunable frequency ranges. Such device may serve in acoustic circuits, like circulators, transducers and imaging systems for rectifying mechanical or acoustic energy flows[15].

Reciprocity is a fundamental principle in wave propagation, requiring the transmission of information or energy between any two points in space to be symmetric for opposite propagating directions[16]. However, devices that break reciprocity, i.e., diodes, are required for rectification and control of the associated energy flow. Unlike electric diodes,

which have led to worldwide revolutions for over a century, mechanical or acoustic diodes are just starting to be explored[15, 17-19]. Achieveing non-reciprocity in mechanical systems through intrinsic time-reversal symmetry breaking has been demonstrated in strongly nonlinear networks[17-19], selective acoustic circulators[20], and topological mechanical insulators[21-23]. Recently, theoretical proposals[10-12] suggested the use of external, spatio-temporal modulation of material's properties as a mean to achieve non-reciprocity.

Experimental realizations of this concept require (i) a dynamic lattice with controllable elastic properties, and (ii) a dynamic modulation with speed comparable to the wave propagation velocity. We meet these requirements by building a mass-spring chain of repelling magnets modulated by externally driven coils. The chain consists of 12 ring magnets ($m = 9.8$ g) free to slide on a supporting smooth cylindrical rail (Fig. 1a, and Methods). To dynamically modulate the chain, we introduce electrical coils around the 8 central ring magnets (masses 3 to 10). The electrical coils are positioned coaxially with the magnets and rest at the same center positions $x_{0,n}$ (Fig. 1a). When a current flows through the electrical coils, they create local magnetic fields that couple to the ring magnets. When the ring magnets are at rest ($x_{0,n}$ position), they sit at the apex of the magnetic potential created by the coils and their coupling forces vanish. When the ring magnets displace, they experience either restoring or repelling forces from the coils, depending on the current direction. The coupling between each pair of ring magnet and coil is similar to a grounding spring. When the grounding spring stiffness is modulated spatiotemporally, time-reversal symmetry is broken leading to the formation of a non-reciprocal bandgap in the dispersion diagram[10-12] (Fig. 1b).

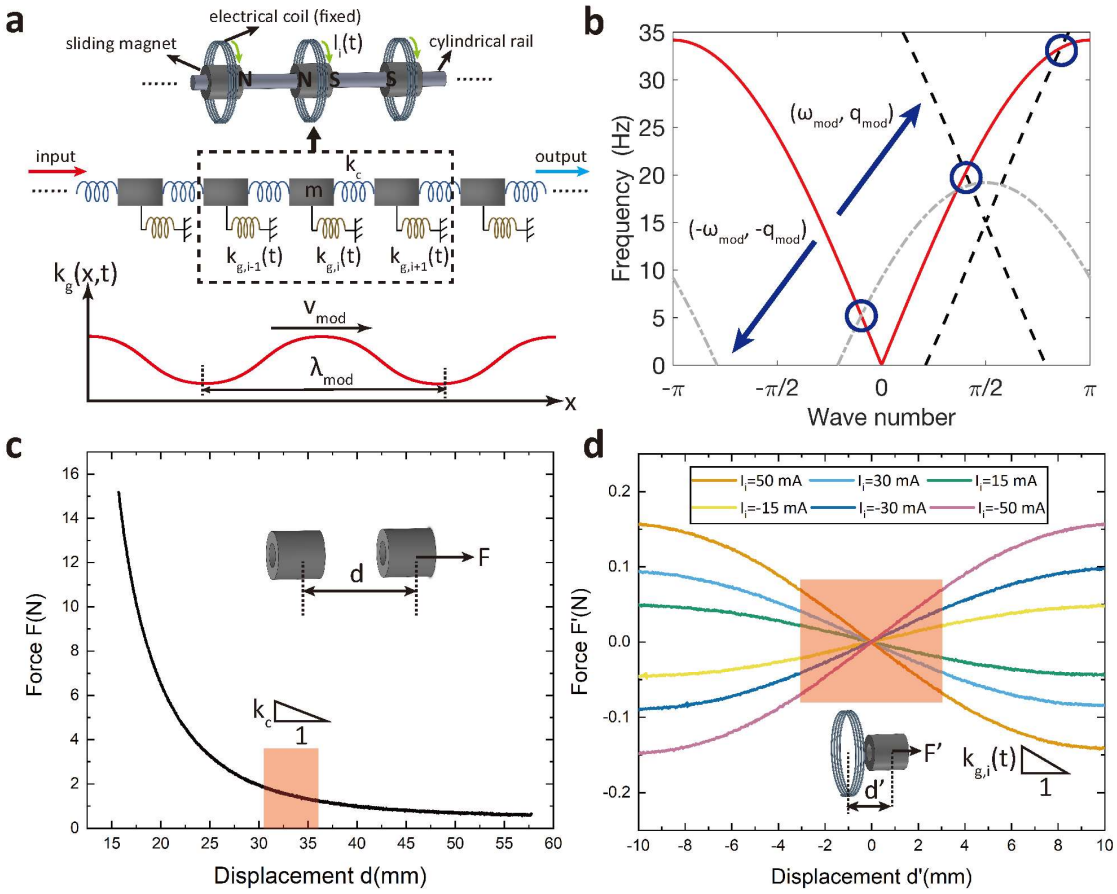

Figure 1 Experimental setup for the non-reciprocal dynamic phononic lattice. (a) Top: Schematic of the experimental setup. Middle: Discrete mechanical representation of the system with masses and springs. Bottom: Schematic illustration of the modulation concept by changing the gounding spring stiffness (k_g) in a wave-like fashion. (b) Scattering analysis: The red solid curve describes the original dispersion relation of the un-modulated monatomic lattice. The black dashed and grey dash-dotted curves correspond to Floquet-Bloch replicas of the original curves obtained by translation along the solid blue arrows $\pm(\omega_{mod}, q_{mod}) = \pm(15\text{Hz}, \pi/2)$. Parity-breaking crossings (circled) are where Bragg's condition is satisfied and non-reciprocal wave scattering is anticipated. (c) Measured force-displacement curve for neighboring magnetic masses. (d) Measured force-dispacement curve between the ring magnet and its surrounding coil at different currents. The red shaded regions in both (c) and (d) corresponds to the dynamic operating regime of our experiments.

To characterize the mechanical parameters of our system, we measure the repelling force between neighboring masses as a function of their displacement (Methods). The resulting force-displacement curve exhibits a nonlinear force that is characteristic of dipole repulsion (Fig. 1c). We also measure the force between the magnets and the surrounding coils at different applied currents (Fig. 1d). To measure the dynamic response of the system, we drive the 2nd mass with a sinusoidal force of frequency f_{dr}, and the velocity of mass 11 is monitored with a laser vibrometer (output signal). The velocity response is measured using a lock-in amplifier as a function of different f_{dr} for different modulation parameters. Due to the small vibration amplitude of the driving signal (≤ 5 mm), the coupling between masses can be approximated by a linear response (Fig. 1c, red shaded area). The linearized coupling stiffness between adjacent magnets obtained from experiments is $k_c \approx 113$ N/m. Similarly the coupling between the electromagnets and the masses can be linearized in the dynamic regime of interest (Fig. 1d). We consider only nearest neighbor interactions between masses and mass-coil pairs, since non-nearest neighbour interactions decay to a negligible amount (Fig. S1).

The spatiotemporal modulation of the system can be achieved by applying sinusoidal AC currents through the coils. Each coil is subjected to a current of the same frequency, f_{mod}, but with a phase shift of $\pi/2$ or $-\pi/2$ between neighbours. The equivalent grounding stiffness for the n-th mass thus can be modelled as:

$$k_{g,n} = k_{g,AC}\cos\left(2\pi f_{mod}t \mp \frac{\pi x_{0,n}}{2a}\right) = k_{g,AC}\cos(2\pi f_{mod}t \mp q_{mod}n)\,, \qquad (1)$$

where $k_{g,AC}$ is the modulation amplitude of the grounding stiffness, $x_{0,n}$ is the equilibrium position of each unit, and $q_{mod} = \pm\pi/2$ is the normalized wave number. Equation (1) describes a traveling wave with wavelength $\lambda_{mod} = 4a$ and speed $v_{mod} = 4af_{mod}$. The modulation amplitude measured in our experiments is $k_{g,AC} = 24$ N/m, which is 21% of the coupling stiffness, k_c.

In the absence of modulation ($k_{g,AC} = 0$), the dispersion relation for an incident small-amplitude plane wave $u_0(n,t) = U_0\exp(i(qn - \omega t))$ is described by $D(\omega, q) =$

$-m\omega^2 + 4k_c \sin^2\left(\frac{q}{2}\right) = 0$. Modulating the lattice harmonically with (f_{mod}, q_{mod}) generates an additional scattered field $u_s(n,t) = U_s \exp\big(i(q_s n - \omega_s t)\big)$ whose mode is *shifted* by an amount (ω_{mod}, q_{mod}) due to spatiotemporal periodicity: $(\omega_s, q_s) = (\omega_0, q_0) \pm (\omega_{mod}, q_{mod})$. The scattered field is negligible however $(U_s \ll U_0)$ except when it is resonant with the incident field; i.e., when the modified Bragg's condition $D(\omega_s, q_s) = D(\omega_0, q_0) = 0$ is met[11]. Graphically, scattered modes are located at crossings between the original $(D(\omega, q) = 0)$ and shifted $(D(\omega_s, q_s) = 0)$ dispersion curves. Note that the crossings are non-symmetrically distributed in a way that breaks parity of the dispersion diagram and, ultimately, reciprocity of wave propagation. Depending on the whether $q_0 q_s$ is positive or negative, the scattered mode propagates either with or against the incident wave, i.e., is either transmitted or reflected. In both cases however, its frequency is shifted away from the incident frequency ω_0. This translates into a one-way dip in the transmission spectrum around ω_0.

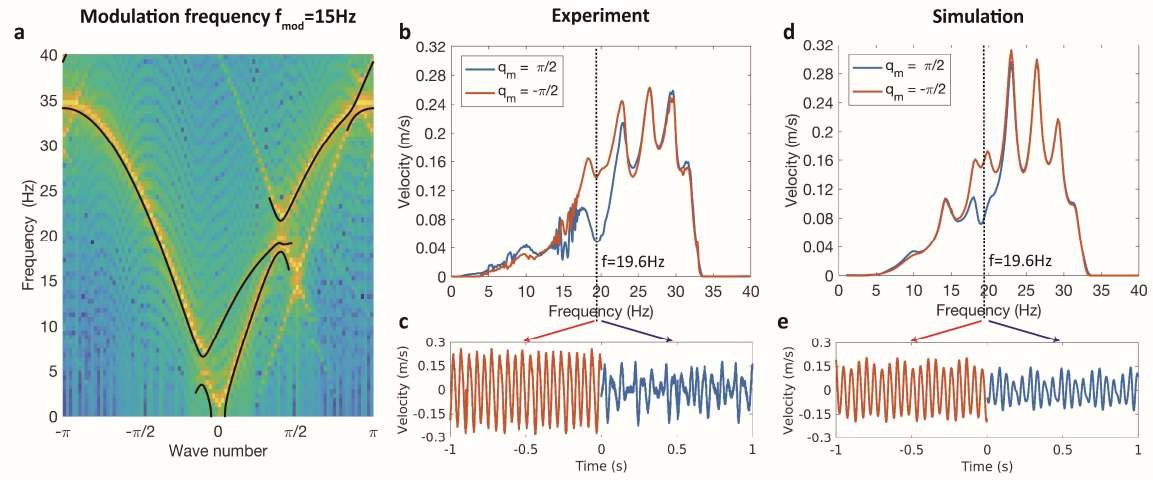

Figure 2 Non-reciprocal wave propagation for $f_{mod} = 15$ Hz. (a) Dispersion diagram of the modulated lattice calculated by Fourier analysis of simulated velocity fields (color map) and analytically by coupled mode theory (solid black line). (b) Measured velocity response function. The amplitude ratio at 19.6 Hz is $r = 2.9$. (c) Measured velocity time series at $f_{dr} = 19.6$ Hz. The time series for $q_{mod} = -\pi/2$ is shown along the negative time axis for better illustration. (d) and (e) are the simulation results corresponding to (b) and (c), respectively. The simulated amplitude ratio at 19.6 Hz is $r = 1.9$ in panel (d).

We first set the modulation frequency to $f_{mod} = 15$ Hz, which falls within the pass band of the monoatomic lattice. For this modulation frequency, three crossings exist at 5 Hz, 19 Hz and 33 Hz and non-reciprocal wave characteristics are anticipated for neighboring driving frequencies f_{dr} (Fig. 2a).

We measure the velocity of the last mass in the array as a function of the driving frequency, f_{dr} (Fig. 2b). The velocity profiles differ when the acoustic waves are traveling in the same (red) or opposite (blue) direction to the modulation wave, at driving frequencies close to $f_{dr} = 19.6$ Hz. We define the co-directional/contradirectional bias ratio as $r = U^-/U^+$ where $U^{\mp}$ denotes the velocity response amplitude for $q_{mod} = \mp\pi/2$. At $f_{dr} = 19.6$ Hz, the measured velocity response profile in time shows that waves traveling in opposite directions have different amplitudes and profiles, with a bias of $r \approx 2.9$ (Figs. 2b, c). The time-domain amplitudes are lower than the amplitudes obtained from the velocity response functions. This is due to the anharmonic nature of the response in the modulated lattice. However, results demonstrate that the signal transfer around $f_{dr} = 19.6$ Hz is strongly enhanced when traveling along the modulation direction and suppressed in the other direction, exhibiting non-reciprocal behavior.

We developed a mathematical model to capture the dynamic characteristics of the modulated lattice. The system can be described as:

$$m\ddot{u}_n + F_{loss} + k_{g,n}u_n + F_{coupl} = \delta_{2,n}A\cos(2\pi f_{dr}t) \qquad (2)$$

for $1 \leq n \leq 12$. Here, $u_n(t) = 0$ at the two boundaries $n = 1,12$. $F_{loss} = b\dot{u}_n + \mu\,\mathrm{sign}(u_n)$ represents dissipative forces within the chain, with viscous damping coefficient $b = 0.056$ kg/s and Coulomb friction coefficient $\mu = 0.012$ N (Methods). The coupling force term is $F_{coupl} = P(a - u_n + u_{n+1}) - P(a - u_{n-1} + u_n)$, where we use the approximation $P(x) = c_1/(x + c_2)^2$ with $c_1 = 0.9788$ mNm^2 and $c_2 = 4.952$ mm obtained from a fitting based on Fig. 1c. $\delta_{2,n}$ is the Kronecker delta which is 1 for $n = 2$ and zero everywhere else. The forcing amplitude $A = 0.21$ N is obtained as a fitting parameter (Methods). The experimental and numerical velocity response functions for a non-modulated lattice agree well (Fig. S2). When the modulation is turned on, the velocity

profiles obtained in experiments and simulations show a similar nonreciprocal response (Figs. 2d, e). However, the non-reciprocal behavior at $f_{dr} = 19.6$ Hz is less pronounced in simulations than in measurements ($r \approx 1.9$).

We computed dispersion curves from space-time Fourier analysis of the velocity field and compared them with the ones obtained with the plane-wave expansion method (Fig. 2a and Methods). The observed non-reciprocal wave characteristics, at $f_{dr} = 19.6$ Hz, agree well with the dispersion characteristics. The dispersion curves (Figs. 1b, 2a) predict non-reciprocal behavior also near 5 Hz and 33 Hz. However, the experimental velocities are too small at these frequencies to capture the effect.

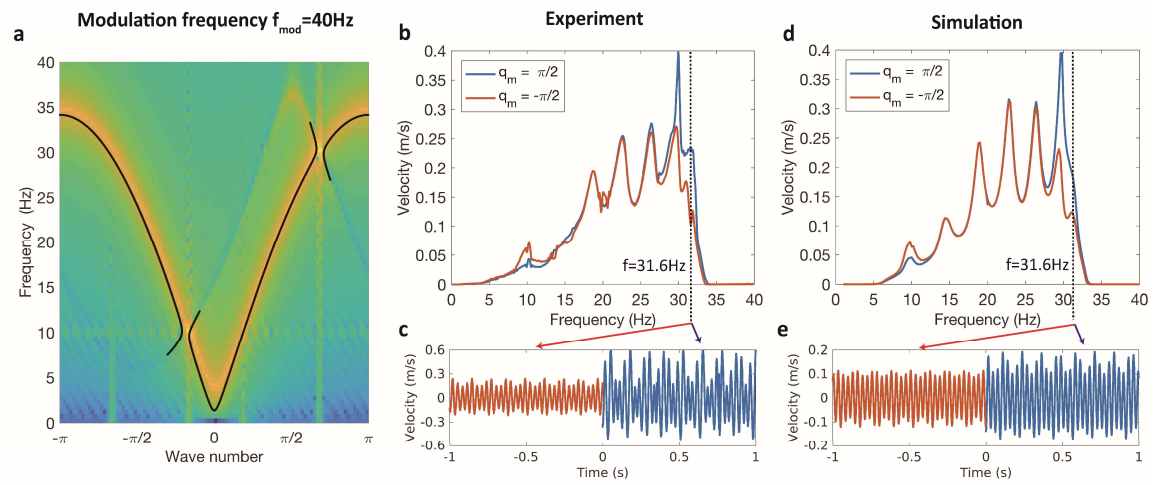

Figure 3. Non-reciprocal wave propagation for $f_{mod} = 40$ Hz. (a) Dispersion diagram of the modulated lattice calculated by Fourier analysis of simulated velocity fields (color map) and analytically by coupled mode theory (solid black line). (b) Measured velocity response function. The amplitude ratios are $r = 1.8$ at 9.8 Hz and $r = 0.4$ at 31.6 Hz. (c) Measured velocity time series at $f_{dr} = 31.6$ Hz. The time series for $q_{mod} = -\pi/2$ is shown along the negative time axis for better illustration. (d) and (e) are the simulation results corresponding to (b) and (c), respectively. The simulated bias ratios are $r = 1.6$ at 9.8 Hz and $r = 0.7$ at 31.6 Hz in panel (c).

In order to demonstrate the tunability of the non-reciprocal frequency range in our system, we next set the modulation frequency to $f_{mod} = 40$ Hz, within the band gap of

the underlying monatomic lattice. Our model predicts non-reciprocal wave behavior for driving frequencies near the crossings at 10 Hz and 30 Hz (Fig. 3a). This is also captured in the measured velocity responses (Fig. 3b) and time domain profiles at $f_{dr} = 31.6$ Hz (Fig. 3c). Corresponding numerical simulations (Figs. 3d,e) agree very well with the measurements.

The dispersion curve of the modulated lattice (Fig. 3a) obtained from numerical calculation corroborates the observed non-reciprocal characteristics for $f_{mod} = 40$ Hz. It reveals two crossings located near 30 Hz and 10 Hz and visible as small bright yellow regions lying on a main dispersion branch. At these points, the modulation-induced scattered field is strong enough to change the overall wave field. This manifests in the velocity response functions as $r > 1$ near 10 Hz and $r < 1$ near 30 Hz. For other points along the main dispersion branch, the scattered wave is too weak compared to the incident field to induce any noticeable non-reciprocal effects. In contrast to the case for $f_{mod} = 15$ Hz, the crossing here occurs between a positive and a negative branch of the dispersion curve ($\omega_0 \omega_s < 0$) and leads to the opening of a couple of "vertical" bandgaps (Fig. 3a). Such crossings are characteristic of unstable interactions[24] caused by supersonic modulation velocities[25] where the velocity field is continuously amplified by drawing energy from the modulation. This explains the presence of the sharp peak around 30 Hz in the transmission spectrum (Figure 3b,d).

Our results provide the first experimental demonstration of modulation-induced non-reciprocity in a phononic lattice. The operating range of our lattice is beyond the asymptotic limits that are typically enforced in the existing theoretical work. The phononic diode developed in our work can be further implemented into micro- or nano-scale electromechanical systems[26,27] with tunable frequencies as basic elements for acoustic rectifying circuits. Since the concept of modulation applies to other types of waves, our results find applications not only to phononic materials, but also to thermal diodes[13], photonic waveguides[14], etc.

Acknowledgements

Y.W., B.Y. and C.D. acknowledge the support from the National Science Foundation under EFRI Grant No. 1741565. H.C., H.N. and G.H. acknowledge support from the National Science Foundation under EFRI Grant No. 1641078. B.Y. acknowledges the support from the National Science and Engineering Research Council of Canada.

Author contributions

Y. W. and C.D designed the experiment. Y.W. performed the experiments. B.Y. performed analytical and numerical modelling of the system. H.C., H.N. and G.H. performed analytical calculations on the dispersion curves. Y.W., B.Y., H.N., G.H. and C.D. wrote the manuscript. All authors interpreted the results and reviewed the manuscript.

Competing Financial Interests

Nothing to report.

Methods

Experimental details

The ring magnets used in our experiment are NdFeB Grade N42 magnets with dimensions of 12.7mm OD, 6.4 mm ID and 12.7mm in length (K&J Magnetics, Inc.). The cylindrical rail is made of fiberglass with diameter 4.76mm. Sleeve bearings made from PTFE with 6.4mm OD and 4.8mm ID and are installed in each ring magnets to fit between magnets and rail and reduce sliding friction. The ring magnets are placed on the rail with the same polarization facing each other, causing them to repel and form a regular one-dimensional lattice. By fixing the two end magnets, the mass chain reaches equilibrium with a uniform spacing $a = 33.4\ \mathrm{mm}$ between neighbours (a is the lattice constant). Electrical coils (APW Company) used in this experiment have dimensions 48.3mm OD, 27.1mm ID and

17.5mm in length, with inductance of 104mH. To measure the force-displacement interaction between two ring magnets and between a magnet and a coil with flowing current, the magnet or coil is fixed on two testing plates of an Instron E3000 materials tester with a 250N load cell. The magnets and/or coil are alighed coaxially and force-displacement curves are recorded for over 3 times and averaged to reduce noise in the data.

To achieve dynamic modulation on the current flowing in the 8 electrical coils, we use electrical signals generated by two synchronized function generators A and B (Agilent 33220A). A phase shift of $\pm\pi/2$ is set between two function generators for forward and backward modulations. The electrical coils #1 and #5 (phase offset 0) are conneted in parallel to function generator A, while coils #3 and #7 (phase offset $\pm\pi$) are conneted to function generator A but with reversed polarization to achieve the π phase shift. Similarly, coils #2 and #6 (phase offset $\pm\pi/2$) are conneted parallel to function generator B, while #4 and #8 (phase offset $\pm 3\pi/2$) are connetcted to B with reversed polarization. The two function generators are set to the same frequency $\mathrm{f_{mod}}$ and amplitude, while the phase shift is set to either $\pi/2$ or $-\pi/2$ for backward and forward modulation directions. The modulation current in each coil is checked with an oscilloscope to ensure same amplitude and phase lag of $\pi/2$ between neighbors. Due to the small cross-inductance and low operation frequency, we do not observe current induced from cross-inductance between neighbors in these coils.

The phononic chain is driven by a separate coil placed off-center from the first moving magnet which is connetcted to a sweeping-frequency lock-in amplifier (Stanford Research SR860). The velocity of the last moving magnet is measured with a laser vibrometer (Polytec CLV-2534).

Simulation of the velocity response curves

The control parameters for experiments are the modulation amplitude $k_{g,AC}$, modulation frequency f_{mod} and driving frequency f_{dr}. The forcing amplitude A may also be controlled by changing the driving current, but it is kept constant in our experiments.

Figure S1 shows the measured and simulated velocity response functions of the un-modulated lattice ($k_{g,AC} = 0$). There is generally very good agreement between measurements and simulations, except for the peak around 15 Hz that is not captured in measurements. This is most likely because the friction forces in experiments are not fully captured by the Coulomb friction model used in simulations. The peaks in the velocity response functions are due to the finite size of the system (waves reflecting from the boundaries) and correspond to different modes of vibration. We observe a sharp cut-off around 33 Hz, which is lower than the cut-off value of $(1/\pi)\sqrt{k_c/m} = 34.3$ Hz based on the dispersion relation. This is due to the presence of energy dissipation[28].

To simulate the velocity response functions for a given set of control parameters, Equation (2) is solved in time until the initial transients decay. For each f_{dr}, the amplitude of motion is then obtained based on the Fourier transform of velocity time series over 500 driving cycles. This procedure reproduces the velocity amplitude measured by the lock-in amplifier. The response of the modulated system is generally not periodic due to the presence of two incommensurate frequencies f_{dr} and $f_{dr} \pm f_{mod}$ (see, for example, Figures 2b and 2d).

We use the velocity response function of the lattice with no modulation ($k_{g,AC} = 0$) to obtain the coefficients of viscous damping b and Coulomb friction μ, as well as the forcing amplitude A. We note that including Coulomb friction is essential for capturing the sharp decay of the velocity response function near the cut off. We used a smooth approximation of the sign function in simulations, $\mathrm{sign}(\dot{u}_n) \approx \tanh(\alpha \dot{u}_n)$ with $\alpha = 1000$.

Data availability. The data that support the findings of this study are available from the corresponding author upon reasonable request.

References

1. Martínez-Sala, R., Sancho, J., Sánchez, J. V., Gómez, V., Llinares, J. & Meseguer, F. Sound attenuation by sculpture. *Nature* **378**, 241 (1995).
2. Page, J. H., Sheng, P., Schriemer, H. P., Jones, I., Jing, X. & Weitz, D. A. Group velocity in strongly scattering media. *Science* **271**, 634 (1996).
3. Vasseur, J. O., Deymier, P. A., Chenni, B., Djafari-Rouhani, B., Dobrzynski, L. & Prevost, D. Experimental and theoretical evidence for the existence of absolute acoustic bad gaps in two-dimensional solid phononic crystals. *Phys. Rev. Lett.* **86**, 3012 (2001).
4. Yang, S., Page, J. H., Liu, Z., Cowan, M. L., Chan, C. T. & Sheng, P. Focusing of sound in a 3D phononic crystal. *Phys. Rev. Lett*. **93**, 024301 (2004).
5. Fang, N., Xi, D., Xu, J., Ambati, M., Srituravanich, W., Sun, C. & Zhang, X. Ultrasonic metamaterials with negative modulus. *Nat. Mater*. **5**, 452-456 (2006).
6. Lu, M. H., Feng, L. & Chen, Y. F. Phononic crystals and acoustic metamaterials. *Mater. Today* **12**, 12 (2009).
7. Matlack, K. H., Serra-Garcia, M., Palermo, A., Huber, S. D. & Daraio. C. Designing perturbative metamaterials from discrete models: from veselago lenses to topological insulators. *Nat. Mater.* **17**, 323-328 (2018).
8. Bilal, O. R., Foehr, A. & Daraio, C. Reprogrammable phononic metasurfaces. *Adv. Mater.* **29**, 1700628 (2017).
9. Bachelard, N. Ropp, C., Dubois, M., Zhao, R., Wang, Y. & Zhang, X. Emergence of an enslaved phononic bandgap in a non-equilibrium pseudo-crystal. *Nat. Mater.* **16**, 808-813 (2017).
10. Swinteck, N., Matsuo, S., Runge, K., Vasseur, J. O., Lucas, P. & Deymier, P. A. Bulk elastic waves with unidirectional backscattering-immune topological states in a time-dependent superlattice. *J. Appl. Phys*. **118**, 063103 (2015).
11. Nassar, H., Chen, H., Norris, A. N., Haberman, M. R. & Huang, G. L. Non-reciprocal wave propagation in modulated elastic metamaterials. *Proc. R. Soc.* A **473**: 20170188 (2017).
12. Vila, J., Pal, R. K., Ruzzene, M., Trainiti, G., A Bloch-based procedure for dispersion analysis of lattices with periodic time-varying properties. *J. Sound Vib.* **406**, 363-377 (2017).
13. Torrent, D., Poncelet, O. & Batsale, J. C. Nonreciprocal thermal material by spatiotemporal modulation. *Phys. Rev. Lett.* **120**, 125501 (2018).
14. Sounas, D. L. & Alù, A. Non-reciprocal photonics based on time modulation. *Nat. Photonics* **11**, 774-783 (2017).
15. Liang, B., Guo. X. S., Tu, J., Zhang, D. & Cheng, J. C. An acoustic rectifier. *Nat. Mater.* **9**, 989-992 (2010).
16. Lamb, H. On reciprocal theorems in dynamics. *Proc. London Math. Soc.* **19**, 144-151 (1988).

17. Li, X. F., Ni, X., Feng, L., Lu, M. H., He, C. & Chen, Y. F. Tunable unidirectional sound propagation through a sonic-crystal-based acoustic diode. *Phys. Rev. Lett.* **106**, 084301 (2011).
18. Boechler, N. Theocharis, G. & Daraio, C. Bifurcation-based acoustic switching and rectification. *Nat. Mater*. **10**, 665-668 (2011).
19. Li, F., Anzel, P., Yang, J., Kevrekidis, P. G. & Daraio, C. Granular acoustic switches and logic elements. *Nat. Comm*. **5**, 5311 (2014).
20. Fleury, R., Sounas, D. L., Sieck, C. F., Haberman, M. R. & Alù, A. Sound isolation and giant linear nonreciprocity in a compact acoustic circulator. *Science* **343**, 516-519 (2014).
21. Wang, P., Lu, L. & Bertoldi, K. Topological phononic crystals with one-way elastic edge waves. *Phys. Rev. Lett.* **115**, 104302 (2015).
22. Serra-Garcia, M., Peri, V., Süsstrunk R., Bilal, O. R., Larsen, T., Villanueva, L. G., Huber, S. D. Observation of a phononoic quadrupole topological insulator. *Nature* **555**, 342-345 (2018).
23. Mitchell, N. P., Nash, L. M., Hexner, D., Turner, A. M. & Irvine, W. T. M. Amorphous topological insulators constructed from random point sets. *Nat. Phys*. **DOI**: 10.1038/s41567-017-0024-5 (2018).
24. Nassar, H., Chen, H., Norris, A. N., Huang, G. L. Non-reciprocal flexural wave propagation in a modulated metabeam. Extreme Mech. Lett. **15**, 97-102 (2017).
25. Nassar, H., Xu, X. C., Norris, A. N., Huang, G. L. Modulated phononic crystals: Non-reciprocal wave propagation and Willis materials. J. Mech. Phys. Solids. **101**, 10-29 (2017).
26. Feng, X. L., White, C. J., Hajimiri, A. & Roukes, M. L. A self-sustaining ultrahigh-frequency nanoelectromechanical oscillator. *Nat. Nanotechnon.* **3**, 342-346 (2008).
27. van der Zande, A. M., Barton, R. A., Alden, J. S., Ruiz-Vargas, C. S., Whitney, W. S., Pham, P. H. Q., Park, J., Parpia, J. M., Craighead, H. G. & McEuen, P. L. Large-scale arrays of single-layer graphene resonators. *Nano Lett.* **10**(12), 4869-4873 (2010).
28. Frazier, M. J., Hussein, M. I. Band structure of phononic crystals with general damping. *J. Appl. Phys.* **108**, 093506 (2010).